INVESTIGATING FAST FOLDING OF RNA PSEUDOKNOT VPK WITH AN ULTRAFAST MICROFLUIDIC MIXER

By

Andreas John Meindl

A THESIS

Submitted to
Michigan State University
in partial fulfillment of the requirements
for the degree of

MASTER OF SCIENCE

Physics

2012

ABSTRACT

INVESTIGATING FAST FOLDING OF RNA PSEUDOKNOT VPK WITH AN ULTRAFAST MICROFLUIDIC MIXER

By

Andreas John Meindl

Despite advances in understanding the theory behind RNA folding, ab initio prediction of the folding process has not been achieved yet. Given only the sequence information we still cannot tell the precise three-dimensional structure of neither RNA nor protein. Knowing the kinetics of folding we hope to learn more about the arrangement of secondary and tertiary structure.

For that reason we investigated the folding process of RNA pseudoknot VPK with our microfluidic mixing device. VPK (variant pseudoknot) is a variant of the mouse mammary tumor virus (MMTV) pseudoknot and it was specifically designed to prevent the formation of alternative base pairings in the stem regions. Using two differently labeled samples, VPK-2AP and F-VPK, and high and low salt folding conditions, we analyzed the folding process and determined the different folding rates. Our results match very well with recently published findings, but they also raise the possible existence of folding transitions not seen in T-jump experiments. The measured folding times are in the range of 0.5 to several milliseconds. The folding process seems to have different pathways with one of the stems of the pseudoknot forming before, perhaps even initiating the folding of the other.

ACKNOWLEDGMENT

Writing a thesis can only prove successful with an interested and motivating mentor and advisor. Therefore, I am very grateful to Lisa Lapidus for the time and effort she invested in instructing me and discussing with me.

I would like to thank my fellow group members for their expertise and the good working atmosphere. Ling Wu introduced me to our setup knowledgeably and laid the base for the success of my work. Terry Ball's help with buffers and the RNA samples was crucial for the good results of the experiments. Srabasti Acharya answered my questions always helpfully, both on general and scientific issues.

The Studienstiftung des deutschen Volkes (German National Academic Foundation) made this wonderful experience of studying abroad possible for me. I am aware of and thankful for their great support, not only in the United States but also during my studies in Germany. At events of the Studienstiftung I have always met the most interesting people. The same holds for events of the Fulbright Association. Bringing people together and giving them the opportunity to make connections is one of the greatest ways to receive encouragement.

I am also indebted to the many friends I made here in East Lansing. Playing all kinds of sports together, having BBQs, watching movies... That doesn't sound like a big thing, but it made life so much more enjoyable.

Last but not least, I would like to thank my family for their ongoing support and guidance in my life. Without you I would not be who I am.

TABLE OF CONTENTS

LIST OF TABLES

LIST OF FIGURES

Chapter 1

Introduction

Ribonucleic acid (RNA) plays an important role in many different processes in molecular biology [1]. The one it is known for the most is as being the intermediate between Deoxyribo nucleic acid (DNA) and protein in gene expression: DNA gets transcribed to messenger (m) RNA by RNA polymerase. Through the cytoplasma of the cell mRNA is transported to the ribosome where the translation takes place and, according to the information of the mRNA, a protein is synthesized.

Besides its messenger function, RNA works as transfer (t) RNA, ribosomal (r) RNA, small interfering (si) RNA and transfer-messenger (tm) RNA in protein translation, thus carrying out different tasks during the process of protein synthesis. Another class of RNAs, ribozymes, possess catalytic capabilities [2]. It is this enzymatic activity that gave rise to the "RNA world" hypothesis stating that RNA molecules were at the origin of life. Being able to both store information and catalyze processes, RNA is thought of being the only molecule needed for a self-replicating system [3].

In addition, RNA is important in virology. Many viruses use RNA to store their genetic information [4]. Therefore, a better understanding of RNA could contribute to find faster ways to prevent further propagation of epidemics like SARS or swine influenza, both of which are caused by RNA viruses [5, 6].

This (incomplete) listing of the roles RNA plays clearly shows its significance. It seems obvious that it will be advantageous for us to know more about this kind of molecule. This thesis focusses on the kinetics of RNA folding. Structure and function are well intertwined not only for proteins but also for RNA molecules. Being able to predict the conformational structure on the basis of the chemical structure could allow the design of new enzymes as well as inhibitors for viruses [1]. Additionally, the folding kinetics seem to be of high importance for the efficiency with which RNA molecules act in a number of biological processes [7].

The subject of the project that led to this master's thesis was to determine the folding kinetics of the RNA pseudoknot VPK with a confocal microscope setup using ultrarapid mixing in a microfluidic chip.

Having provided the motivation for studying RNA in the introduction, I will give some background information on RNA and protein folding in the second chapter. The third chapter focuses on experimental methods used for investigating fast folding with an emphasis on the methods we use. In the fourth chapter the results of the folding experiment are presented and discussed. Finally, the fifth chapter provides a short summary and an outlook on further possible experiments.

Chapter 2

Theory

With our setup we are able to investigate both RNA and protein folding. The term folding (of either RNA or protein) refers to the process of finding the correct 3-dimensional structure in order to obtain the biologically active state [8]. Although the governing forces are quite different for protein and RNA folding, the basic principles are comparable and experimental methods to determine the kinetics of the folding process are often the same. The basic theory of this process will be laid out in this chapter.

Protein folding has been investigated since Anfinsen discovered in the 1950s that it is mainly the amino acid sequence of a protein that determines its three-dimensional structure [9]. Misfolded proteins are believed to cause diseases like bovine spongiform encephalopaty (BSE), human Creutzfeld-Jacob disease and Alzheimer's disease [10, 11]. The importance of understanding RNA folding has already been emphasized in the first chapter. Since neither protein nor RNA folding is completely understood, this short overview will only be based on the current state of scientific knowledge, and considerably more is known about protein

than RNA folding.

2.1 RNA folding

RNA is built up from a sequence of four different nucleotides: adenine, cytosine, guanine and uracil, often referred to as A, C, G and U. These nucleotides form single strands by binding covalently to each other. Just as for DNA it is favorable for RNA to form Watson-Crick base pairs between A and U (i.e. thymine for DNA) and C and G, respectively. Since complimentary parts of the sequence are likely to pair, normally the RNA is not in an extended but in a folded configuration [1]. Also, since every single nucleotide carries a phosphate group with a negative charge, ions in the solvent play an important role for the folding process [12].

The sequence information is referred to as the primary structure. Secondary structure describes the Watson-Crick base pairs that form as a consequence of available hydrogen bonds, base stacking and electrostatic interactions. Double stranded RNA forms double helices just as DNA does. The secondary structure motifs RNA can form are hairpins, bulges, internal loops and junctions. Finally, tertiary structure characterizes how secondary structures orient with respect to each other. The RNA we investigated for this thesis forms a pseudoknot. This is essentially a hairpin loop that base-pairs with a later part of the sequence. Other tertiary structures include for example loop-loop interactions [13].

RNA folding is believed to be a hierarchical process, meaning that secondary structure forms early during folding, and tertiary structure only orients the secondary structure elements afterwards [1]. Figure 2.1 shows a simplified folding pathway of RNA. Here, inter-

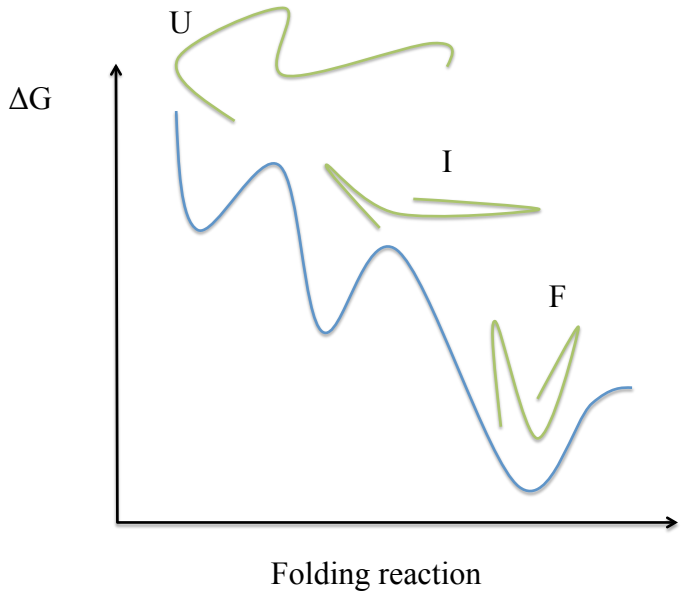

Figure 2.1: Simplified view of a folding reaction. The unfolded state (U) is energetically unfavourable. The native, i.e. folded state (F) minimizes ΔG. During the folding process the molecule can get trapped in (multiple) local minima of the energy landscape. These conformations are called intermediate states (I). For interpretation of the references to color in this and all other figures, the reader is referred to the electronic version of this thesis.

mediate states (commonly referred to as I or IS), that could trap the RNA in a non-native state, may show up.

2.2 Folding kinetics

Perhaps the easiest way the folding process can be thought of is a transition within a two-state model. This approach is valid under the condition of rapid equilibration of the unfolded conformations before folding takes place [14]. The two-state model has a denatured or unfolded (U) state and a native or folded (F) state. These two states are in equilibrium

with each other and knowing the folding and unfolding rates k_f and k_u, we can calculate the equilibrium constant K_{eq} and the difference in the Gibbs free energy, ΔG, which is a measure of the stability of the folded protein [15]:

$$F \underset{k_f}{\overset{k_u}{\rightleftharpoons}} U \tag{2.1}$$

$$K_{eq} = \frac{k_u}{k_f} \tag{2.2}$$

$$\Delta G_{unfold} = -RT \ln K_{eq} \tag{2.3}$$

with R the universal gas constant and T the absolute temperature. ΔG can also be written as:

$$\Delta G_{unfold} = \Delta H - T\Delta S \tag{2.4}$$

with ΔH and ΔS the change in enthalpy and entropy, respectively. Equation 2.4 elucidates that folding is an interplay between entropy and enthalpy. When a protein folds, the number of possible configurations is reduced, i.e. S decreases unfavorably. Therefore folding can only occur when at the same time enthalpy decreases by the forming of energetically favorable contacts between nucleotides [16].

In terms of folding time τ_f, equation 2.3 can be written as:

$$\tau_f = \tau_f^0 \cdot \exp\left(\frac{\Delta G_F}{k_B T}\right) \tag{2.5}$$

where ΔG_F is the height of the free energy barrier and τ_f^0 a prefactor which can be approx-

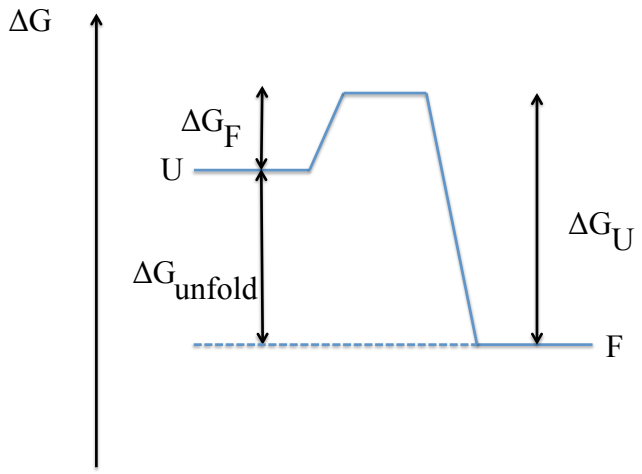

Figure 2.2: Unfolded (U) and folded (F) state separated by an energy barrier. Depending on the side of the barrier, the former may seem higher or lower, which leads to different folding/unfolding rates.

imated by the Kramer's theory of reaction rates.

However, our experiments are not carried out in equilibrium. The observed folding rate k_{obs} is the sum of the folding and unfolding rate:

$$k_{obs} = k_u + k_f \tag{2.6}$$

where k_u and k_f arise from transition state theory: the rate at which one state converts to another from which it is separated by a certain energy barrier, ΔG_U and ΔG_F, respectively, is dependent on this activation energy barrier. A graphic description can be seen in figure 2.2.

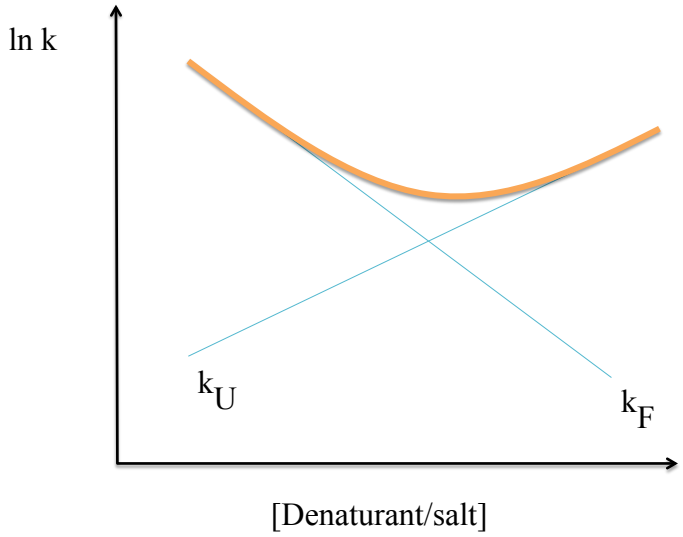

Figure 2.3: Typical plot of the logarithm of the observed folding rate k versus concentration of denaturant or salt, respectively, for a two-state model. The orange line ("chevron") represents the observed folding rate, the blue lines show the linear relationship between the logarithm of the (un)folding rate and the exponent of equation 2.7.

According to transition state theory k_u and k_f can be described by:

$$k_{u(f)} = k^0_{u(f)} \cdot \exp\left(\frac{-\Delta G_{U(F)}}{k_B T}\right) \tag{2.7}$$

with $k^0_{u(f)}$ the unfolding (folding) rate in water, and $\Delta G_{U(F)}$ the height of the free energy barrier. As a consequence of equation 2.6, typical plots of folding rates versus the concentration of denaturant or salt, respectively, look like a chevron (figure 2.3).

Equations 2.2 and 2.3 are valid not only for two-state models, but also for models with intermediates [15] and can be regarded as a universal approach to the folding problem [17]. By calculating the energy of not only two, but of many intermediate states as well, we can

draw an energy landscape. This energy landscape is like a rugged funnel through which RNA or protein has to go upon folding and in which it sometimes gets trapped in intermediate states. Rather than being well-defined, intermediate states often resemble an ensemble of states [18]. Beauchamp et al. recently investigated whether the two-state model describes protein folding well [19]. Based on 14 different protein folding simulations their conclusion is that the two-state model is a reasonable approximation of the folding process.

2.3 Protein folding

All the equations in the last section hold for RNA and protein folding. Only the governing principles are different, since the structures of RNAs and proteins differ.

The primary structure of proteins is a sequence of 20 different amino acids. As opposed to RNA, some amino acids carry either a positive or a negative charge, and some are electrically neutral. Proteins consist of from a few tens to thousands of amino acids. The protein titin, for example, is made up of around 30,000 amino acids [20]. Amino acids not adjacent in the sequence interact with each other via hydrogen bonds and electrostatic interactions. This and the hydrophobicity of some of the amino acids leads to the forming the secondary structure. The most common motifs are α-helices, β-sheets and connecting loops [8]. Tertiary structure, again, is the spatial orientation of these secondary structure elements.

2.4 Computational approaches to RNA and protein folding

Soon after the structure of proteins was discovered the so called *Levinthal Paradox* became apparent [21]: The molecules find their unique structure in a much shorter time than needed for an entropic search through all possible conformations. Despite advances it still remains most challenging to simulate the folding process. Simulating 1 nanosecond still takes around one day for a supercomputer [22].

Progress has been achieved by both new algorithms and better hardware. New techniques and better algorithms, e.g. more exact force fields and coarse-grained models, speed up the simulation of protein folding. Recently Lindorff-Larsen et. al. published a study showing their results of all-atom molecular dynamics (MD) simulations for 12 different protein domains and comparing them in a consistent way [23]. These simulations were run on a specifically designed parallel supercomputer called "Anton" [24]. The project "Folding@home" follows a distributed computing approach that uses idle time of participating personal computers to obtain more and more computational power [25]. Therefore all-atom MD simulations for large proteins might be feasible in a reasonable amount of time not too far away in the future [26].

However, since the big breakthrough in understanding protein folding has not occurred yet, further experiments are still necessary, not least for the validation of computational results.

2.5 Experimental approaches to RNA and protein folding

RNA and protein folding is still a huge challenge to investigate and also to computationally simulate. In order to reduce complexity fast-folding proteins with folding times shorter than 100 μs have become the focus of attention [27]. In general folding can be initialized by chain synthesis, the application of forces to the ends of the molecule or by changing the chemical environment, i.e. the solvent [28]. For fast-folding experiments the latter is the preferred method. There are different ways to change the solvent condition, e.g. photochemical triggering, temperature- or pressure-jump, and ultrarapid mixing [29]. For our experiments described in this thesis we used ultrarapid mixing and later on we will compare our results with temperature (T)-jump experiments. Both of these methods will be described in chapters 3.2 and 3.4, respectively.

Chapter 3

Experimental methods and setup

Our setup is an ultrarapid mixing device making use of confocal scanning microscopy and microfluidics. In this chapter I am going to present the concepts behind confocal microscopy and hydrodynamic mixing through focusing, before the experimental setup used for the experiments is described. Finally the idea behind laser temperature jump (T-jump) is explained and the differences between T-jump and our experiments are laid out.

3.1 Confocal microscopy

In confocal microscopy high resolution is obtained by minimizing stray light coming from points out of focus. This is achieved by using a small pinhole in front of the detector. In addition the light source, typically a laser, is focused on the point of interest and illumination of other points is reduced. The term *confocal* refers to the point of interest being in the focus of both the lens focusing the laser onto the sample and the lens focusing the light signal coming from the sample on to the detector. Using a beamsplitter a single lens can be used

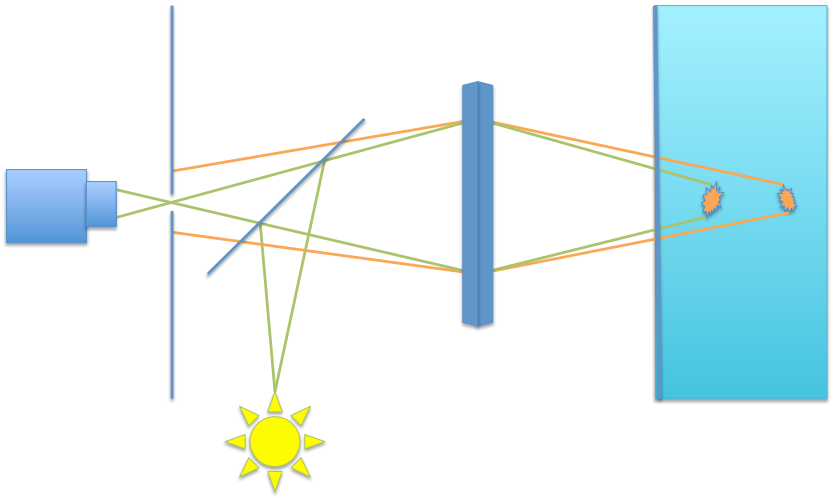

Figure 3.1: Schematics of epitaxial confocal microscopy. Point illumination excites only fluorophores in the focal volume. Stray light from points out of focus (orange line) is blocked by a pinhole. These two measures increase the signal-to-noise ratio significantly.

for both purposes as it is shown in figure 3.1. This is called *epitaxial* confocal microscopy, since light source and detector are on the same side of the sample [30].

Theoretically the resolution R of a diffraction limited microscope is given by the Rayleigh criterion [31]:

$$R = \frac{0.61 \cdot \lambda}{NA} \tag{3.1}$$

where λ is the wavelength of the illuminating light and NA the numerical aperture. This limit is referring to the case where the first diffraction minimum of one source point coincides with the maximum of another.

Confocal microscopes have a slightly higher resolution due to only pointwise illumination

of the sample. The theoretical resolution then is approximately [32]:

$$R_{confocal} = \frac{0.4 \cdot \lambda}{NA} \tag{3.2}$$

For our argon ion laser at $\lambda = 258\,\text{nm}$ and a numerical aperture of 0.5, as used in our experiment, this results in an optical resolution of $R \approx 200\,\text{nm} = 0.2\,\mu\text{m}$. Even so, the manufacturer of the objective used in our setup states a maximum resolution of only $1\,\mu\text{m}$.

3.2 Microfluidic mixing

Mixing is most often associated with turbulence. In order to achieve shorter mixing times, however, turbulent mixing it is not necessarily the best way [33]. Hydrodynamic focusing in microfluidic devices uses the laminar flow regime to mix solutions quickly and in a controlled manner.

A way to differentiate between turbulent and laminar flow is the Reynolds number. It is defined as the ratio between viscous and inertial forces and, for a flow it can be simplified to [34]:

$$Re = \frac{u \cdot D_h}{\nu} \tag{3.3}$$

where u is the velocity, ν the kinematic viscosity and D_h is the hydraulic diameter. The latter is essentially the diameter of the passage. For Reynolds numbers lower than 100 the flow is laminar, the transition to turbulent flow occurs at around $Re \approx 2000$ [35]. Therefore using very small channel dimensions allows work in the laminar flow regime. Applying equation 3.3 to our setup, for a kinematic viscosity of around $10^{-6}\,\text{m/s}^2$ for water at room

temperature, a typical flow speed of 1 m/s and channel dimensions of 10 μm, the Reynolds number equals 10. Therefore the flow conditions in our microfluidic chip are well in the laminar flow regime.

Hydrodynamic focusing takes advantage of the laminar flow regime where mixing happens in a diffusive manner. In our microfluidic mixer a flow through the center channel gets compressed or "focused" by two side channels to 100 nm. Figure 3.2 shows schematically the mixing region of the ultrafast microfluidic mixer used in our setup. Typically the center channel contains the sample, either protein or RNA, in denaturant solution, i.e. it is in the unfolded state. The buffer in the side channels compresses the flow to a small jet of sample material. Due to the small dimensions of the channels this happens at low Reynolds numbers and no turbulent mixing takes place. The mixing is completed when the buffer has diffused through the jet. Therefore the smaller the jet, i.e. the stronger focused it is, the shorter the mixing time. Furthermore, knowing the diffusion constant we can tell precisely when the mixing is complete, and different positions downstream on the jet refer to different points in time after mixing.

3.3 Experimental setup

Our experiments were conducted on a custom built confocal microscope combined with a microfluidic mixer, as described by Lapidus et al. [36]. As pictured in figure 3.3, an argon ion laser (Lexel Laser 95-SHG, Lexington, KY) at 254 nm is focused on the sample via a $0.5NA$ UV objective (OFR LMU-40x-UVB, Newton, NJ) with a focal spot of 1 μm diameter. Emitted fluorescence light is separated from excitation light via a dichroic mirror (Chroma

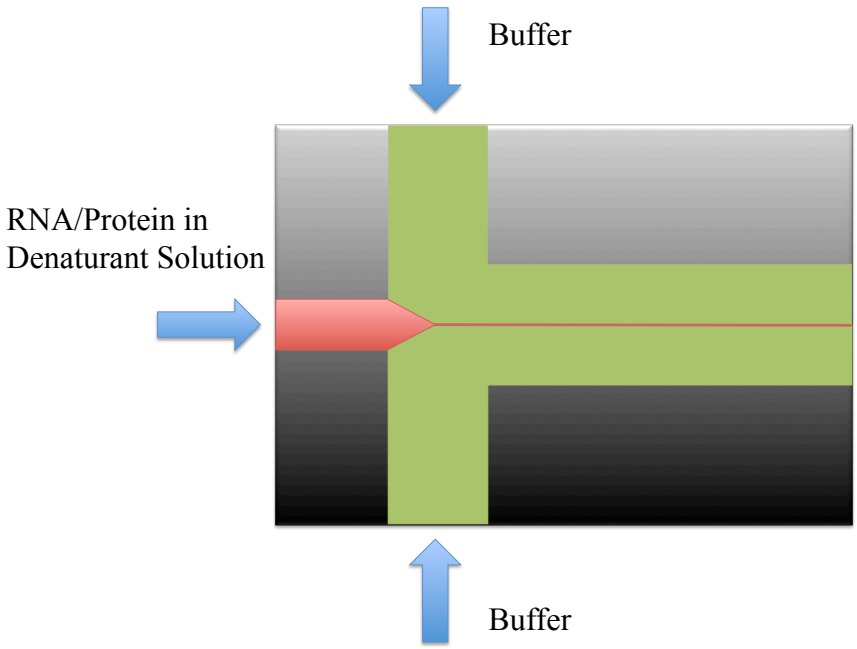

Figure 3.2: Schematics of our mixing chip. Flow through the center channel containing RNA/protein in denaturant solution gets compressed ("focused") by two side channels containing buffer, and a jet of center channel solution is formed. Sandwiched by buffer the RNA/protein solution flows down the mixing channel. Buffer diffuses quickly into the tiny jet, and different positions behind the mixing region can be assigned different points in time after mixing, thus allowing a time resolved investigation of the folding kinetics.

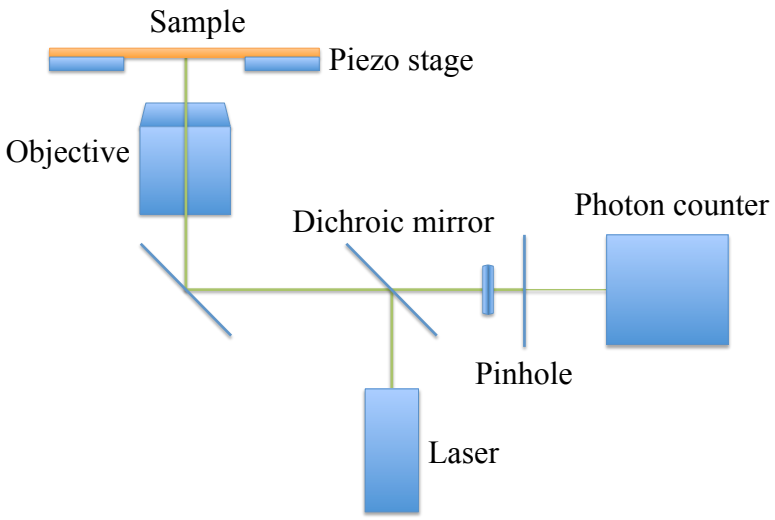

Figure 3.3: Schematics of our setup. Excitation light coming from the laser is focused on the sample by the objective. Emitted fluorescence light is collected by the same objective and, after passing through a dichroic mirror, focused on the pinhole before hitting the photon counter.

300dclp, Brattleboro, VT) and and collected with a photon counter (Hamamatsu, H7421-40, Hamamatsu City, Japan). Note that by focusing the light on a 100 μm pinhole in front of the detector stray light gets blocked and only light from the small focal volume reaches the detector. This allows the use of a "simple" photon counter that only measures fluorescence intensity. Alternatively we can use another argon ion laser (Melles Griot IMA1, Carlsbad, PA) at 488 nm with a flip mirror, thus being able to work with ultraviolet fluorescence at 254 nm as well as visible light at 488 nm. The objective then is a 1.2 NA water immersion objective (Olympus UPlanSApo 60xW, Tokyo, Japan). Images are acquired by scanning the chip over the objective with a three-axis piezoelectric scanner (Mad City Labs Nano-LP100, Madison, WI).

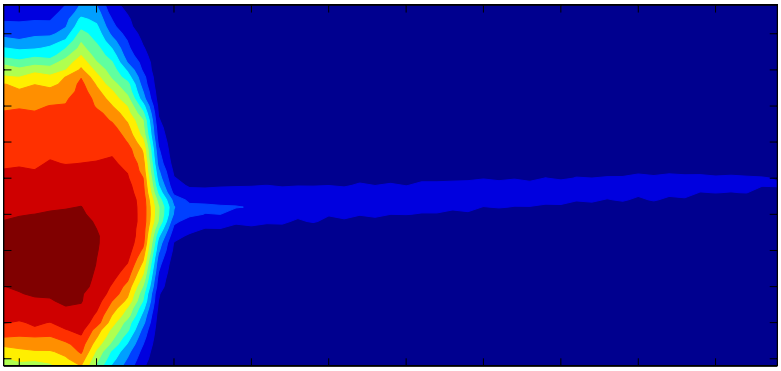

Figure 3.4: Mixing region of the microfluidic mixer. From the left the center channel solution flows into the mixing region, where a tiny jet is produced by pressure applied via the side channels coming from the top and bottom. On forming the jet the signal drops sharply. The focussed jet proceeds through the exit channel. The dimension of this scan is $50 \times 10\,\mu$m.

The basic design of our mixing chip was developed by Knight et al. [33] and optimized by Hertzog et al. [37]. Fig. 3.4 shows a typical scan of the mixer used for the experiments. The depth of the channels is $10\,\mu$m and the length of the exit channel, where the measurements are done, is $500\,\mu$m. The width of the exit channel is $10\,\mu$m. The flow through the center channel is hydrodynamically focused to a jet by the flow through the side channels. The width of the produced jet is about 100 nm (however, our optical resolution is only about $1\,\mu$m). Flow rates used in our experiments range from around 0.1 to 1 m/s and the mixing time, depending on the flow rates, can be as short as $8\,\mu$s [36]. The lowest flow rate we used for our experiment was 0.125 m/s. Therefore, with the exit channel being $500\,\mu$m in length, the latest point in time after mixing we observed is 4 ms.

The chip is mounted on a manifold whose temperature can be controlled via two Peltier elements (TE Technology CH-77-1.0-0.8, Traverse City, MI). Thus we are not only able to conduct experiments at room temperature, but also at higher temperatures allowing us to

reach different regions of the energy landscape of the folding process. The manifold also incorporates reservoirs for the different solutions. Computer controlled pressure transducers (Marsh Bellofram Type 2000, Newell, WV) apply air pressure on these reservoirs in order to obtain the desired flow speeds.

Folding can be observed as a change in fluorescent signal from the jet. The molecules under observation are either intrinsically fluorescent or have some fluorescent labels attached. In certain structural conformations quenching occurs, i.e. quantum yield, and therefore fluorescent intensity decreases. This allows to deduce in which conformational state, folded or unfolded, the molecules are. Most important to us, even if we don't know the exact configuration, the change in signal intensity tells us about the kinetics of the folding reaction.

In order to differentiate between loss in fluorescence intensity due to diffusion out of the jet and due to a change in conformation, respectively, we have to take control measurements without the salt in the side channels. We then analyze the ratio of the intensities from the folding and control measurements along the jet. This ratio should reveal characteristic folding kinetics by comparing it with equilibrium fluorescence data. Another advantage of taking the ratio is to overcome the signal drop in the mixing region due to the forming the jet (cf. figure 3.4).

3.4 Temperature jump

Laser temperature jump (T-jump) is a method that investigates kinetic processes of biological macromolecules. Starting from equilibrium a system gets disturbed by a rapid rise in temperature. This disturbance is most often a short laser pulse that heats up the sample. In

order to gain a high temporal resolution, the laser pulse has to be short. However, it should be powerful enough to change the equilibrated system significantly. After the pulse the relaxation of the system can be monitored, e.g. by UV absorption or fluorescence intensity. Because of the high temporal resolution of this technique it is very well suited for ultra-fast folding molecules [38].

3.5 Difference in T- and ion-jump experiments

T- and ion-jump experiments both investigate the kinetics from a non-native to the native state. However, the trigger for starting this transition differs for the two methods. In T-jump experiments a sudden change in temperature disturbs an equilibrated system. The deviation from the equilibrium by the T-jump is dependent on the change in temperature. Speaking in terms of an energy landscape for folding processes, the bigger the jump, the farther away the system gets from its original state.

Our setup is an ion-jump experiment. Ultrarapid mixing represents an abrupt change in solvent environment for the RNA. After mixing the system is observed while it is equilibrating. Since the sample is first in denaturant without salt, it is completely unfolded and in an extended conformation due to its intrinsic negative charges.

This difference in starting conditions for the two methods is crucial. Biyun et al. studied the difference of the two methods in a coarse grained molecular dynamics simulation of a pseudoknot found in human telomerase [39]. For ion-jump experiments electrostatic interactions lead to a very fast folding process at timescales of a few hundred microseconds. On the other hand, for T-jump experiments non-bonded tertiary interactions, which are weaker

compared to electrostatic interactions, play a major role. One of the results of their simulation is that folding after ion-jump usually happens faster than after T-jump. In their specific case of the human telomerase RNA pseudoknot, the first phase of folding happened five times faster for ion jump than for T-jump, and the slower phase took only half the time.

However, Narayanan et al. recently reported folding/unfolding kinetics of a nucleic acid hairpin investigated by both laser T-jump and ion-jump (ultrafast mixing with counterions), with folding rates for ion-jump as much as 10 times slower than for T-jump [40]. This might be due to the fact that in ion-jump experiments nucleic acids collapses very quickly and the subsequent kinetics are mainly dominated by a transition from the collapsed to the folded state.

Chapter 4

Folding kinetics of RNA pseudoknot VPK

In general, pseudoknots as a minimal motif in secondary structure of RNA play a crucial role in many biological processes, such as translational frameshifting and gene expression and replication [7, 41, 42]. As mentioned earlier, small, fast-folding molecules are interesting objects to study due to their lower complexity. The folding process is less complicated and easier to reconstruct. The following chapter presents the results of our experiments on the folding kinetics of RNA pseudoknot VPK, which is a variant of the mouse mammary tumor virus (MMTV) mRNA.

4.1 Experimental details

The setup we used for the experiments was described in chapter 3.3. We conducted experiments with two different samples. One was pseudoknot F-VPK labeled with fluorescein at the

5'-end. The other one was VPK-2AP with one nucleic acid substituted with 2-aminopurine (2-AP). 2-AP is a fluorescent analog of adenine and guanine, allowing to investigate the structure and kinetics of RNA and DNA, respectively [43]. In our sample, a gift from the Ansari group at the University of Illinois at Chicago, only a single adenine base is replaced by 2-AP (cf. figure 4.1). These two samples highlight slightly different features of the folding process, since the fluorescence signal comes from different positions in the secondary structure: the fluorescein label is attached at one end of the pseudoknot, 2-AP is at position 20 of the RNA chain. Although the fluorescence signal under folding might look different for the two samples, the derived kinetics from both samples should be the same if the relatively large fluorescein label has no impact on the folding process.

For the experiments, both samples were dissolved in 8 M urea, a strong denaturant. Urea prohibits hydrogen bonding between RNA strands, i.e. the forming of secondary structure, by making hydrogen bonds with the RNA bases itself [44]. Therefore, before mixing the RNA in the center channel is in an unfolded, extended conformation, not least because no counterions are present in order to prevent the nucleotides from repelling each other due to their negative charge.

The side channels contained either 10 mM sodium cacodylate (NaC) with 1 M sodium chloride (NaCl) or 10 mM 3-(N-morpholino)propanesulfonic acid (MOPS) buffer with 50 mM potassium chloride (KCl), from now on referred to as NaC and MOPS, respectively. These two different folding environments allow us to compare our results with recently published papers [7, 45]. The low salt concentration in MOPS is a more physiological environment, the high salt concentration in sodium cacodylate buffer is closer to the simulated conditions by Cho et al. [45]. The salt in the side channels provides a charged environment. These

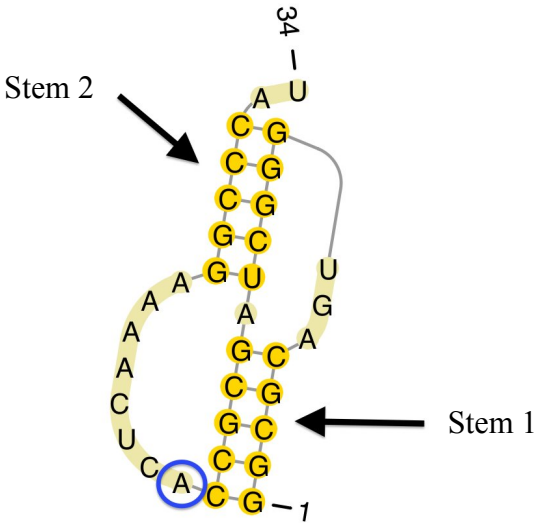

Figure 4.1: Secondary structure of RNA pseudoknot VPK. F-VPK is labeled with a fluorescein molecule at the 5'-end (the label is not shown in this figure). Stem 1 and 2 are the regions of the structure where base pairing occurs. Nucleotides involved in base pairing are highlighted in dark yellow, nucleotides in a loop in light yellow. The circle marks the position where adenine is replaced by 2-AP for VPK-2AP. A stands for adenine, C for cytosine, G for guanine and U for uracil.

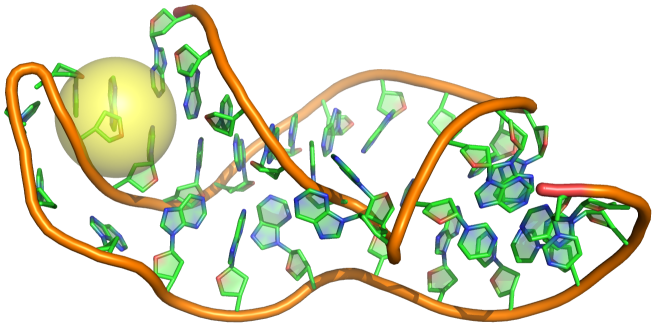

Figure 4.2: Tertiary structure of RNA pseudoknot VPK. The residue marked by the yellow sphere is replaced by the fluorescent nucleic acid analogue 2-aminopurine (2-AP) for VPK-2AP.

counterions are crucial for the RNA to fold, since all the single nucleic acids are negatively charged and would repel each other otherwise.

Briefly, we mix unfolded RNA in folding buffer and observe the folding process.

4.2 Results

We investigated folding kinetics for the two slightly different samples (F-VPK and VPK-2AP) and two folding conditions (NaC and MOPS) at up to 7 different temperatures.

A typical fluorescence intensity curve for F-VPK in NaC is shown in figure 4.3a. It shows a steep rise shortly after mixing and a slower decay afterwards. We normalized the data, so that for $t < 0$, i.e. before mixing, the intensity ratio of control and folding experiments is 1. The fact that the intensity ratio shortly after mixing is constantly above 1 for all measurements, is a clear sign for an early folding process within and shortly after our mixing

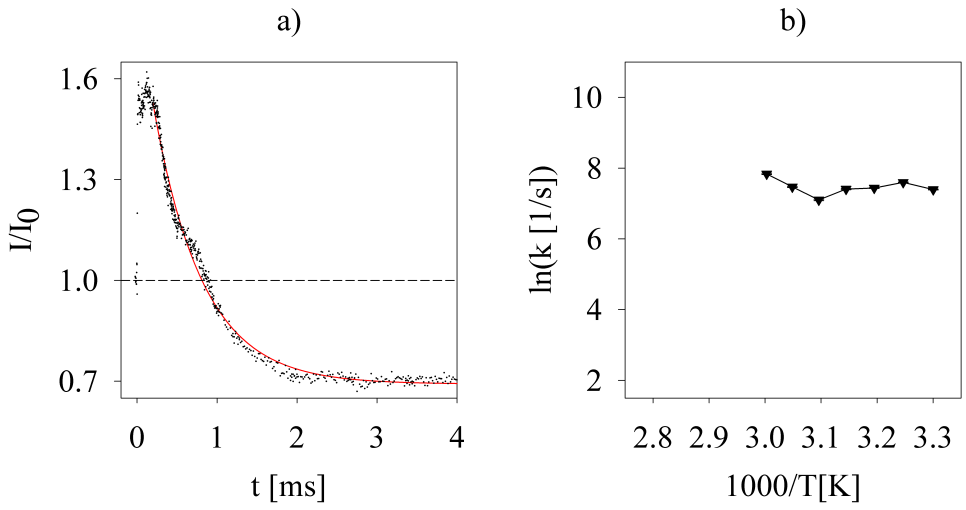

Figure 4.3: a) Intensity curve for F-VPK in sodium cacodylate at 30 °C. The plot (black dots) shows the ratio of our folding and control measurements (without counterions). The dashed line represents the ratio of the premixing amplitudes. The fit (red line) is a single exponential decay for the data after 200 μs giving a characteristic folding time of $614 \pm 8\,\mu$s. Before 200 μs a rise can be seen, but we are unable to resolve it in terms of folding time. Apparently, the folding process starts early and conformational changes happen already within mixing time ($\approx 10\,\mu$s). b) Arrhenius plot for F-VPK in MOPS. The downwards pointing triangles stand for a fitted exponential decay. The folding rate is almost constant.

time. Although we can clearly see that an early folding event is happening, we are not able to resolve it. Experiments were done at seven different temperatures from 30 °C to 60 °C in steps of 5 °C.

For the kinetic measurement of F-VPK in sodium cacodylate we fitted every curve to a single exponential decay to the data after 200 μs. Fitting the data only after this point in time gave the best results for fitting a single exponential to the decay. The resulting folding rates and times can be seen in table 4.1. Figure 4.3b shows the Arrhenius plot for the different temperatures, revealing that the folding rate is almost independent of temperature.

Table 4.1: Folding rates and times for F-VPK in NaC based on a single exponential fit excluding data points before 200 μs.

T in °C	k in 1/s	Δk in 1/s	τ_f in s	$\Delta\tau$ in s
30	1630	20	6.15E-04	7.E-06
35	1990	20	5.02E-04	5.E-06
40	1700	20	5.89E-04	7.E-06
45	1650	30	6.07E-04	9.E-06
50	1210	20	8.3E-04	2.E-05
55	1750	30	5.70E-04	9.E-06
60	2530	50	3.95E-04	7.E-06

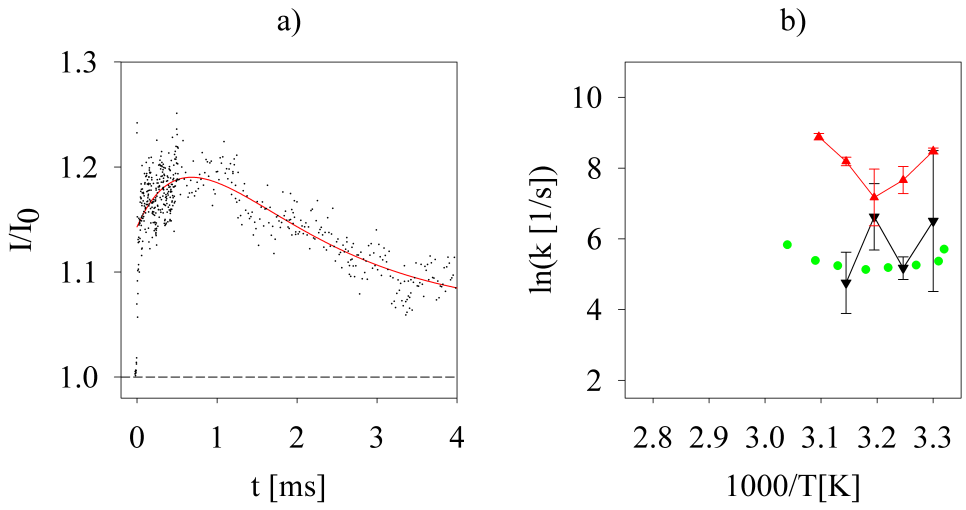

Figure 4.4: a) Intensity curve for F-VPK in MOPS at 40 °C. The plot shows the ratio of our folding and control measurements (without counterions). The fit (red line) is a double exponential fit. The data shows a fast rise in intensity followed by a slower decay. b) Arrhenius plot for F-VPK in MOPS. The downwards (upwards) pointing triangles stand for a fitted exponential decay (formation). Considering the error bars the two folding rates seem to be constant. The green circles are data points published by Narayanan et al. [7].

The experiments done with F-VPK in MOPS showed a similar behavior. However, the overall signal for the MOPS measurements was weaker compared to measurements in NaC resulting in larger uncertainties in the fitted functions. In figure 4.4a a typical curve for F-VPK in MOPS can be seen. Compared to F-VPK in NaC the fast formation process happens later, so that we are actually able to analyze it. This gives us two different rates for the fast formation and a slower decay in the intensity curves. The exact data is shown in table 4.2. The corresponding Arrhenius plot can be seen in figure 4.4b.

Table 4.2: Folding rates and times for F-VPK in MOPS based on a double exponential fit to the data. All points after 10 μs were included for the fit. The data obtained for 55 and 60 °C were not fitted due to its noisiness.

	T in °C	k in 1/s	Δk in 1/s	τ_f in s	$\Delta\tau$ in s
fast rate	30	4800	400	2.1E-04	2.E-05
	35	2100	800	5.E-04	2.E-04
	40	1000	1000	8.E-04	6.E-04
	45	3600	400	2.8E-04	3.E-05
	50	7200	700	1.4E-04	1.E-05
	55	-	-	-	-
	60	-	-	-	-
slow rate	30	1000	1000	2.E-03	3.E-03
	35	180	60	6.E-03	2.E-03
	40	800	700	1.E-03	1.E-03
	45	100	100	9.E-03	7.E-03
	50	0.4	300	2.46	2.E+03
	55	-	-	-	-
	60	-	-	-	-

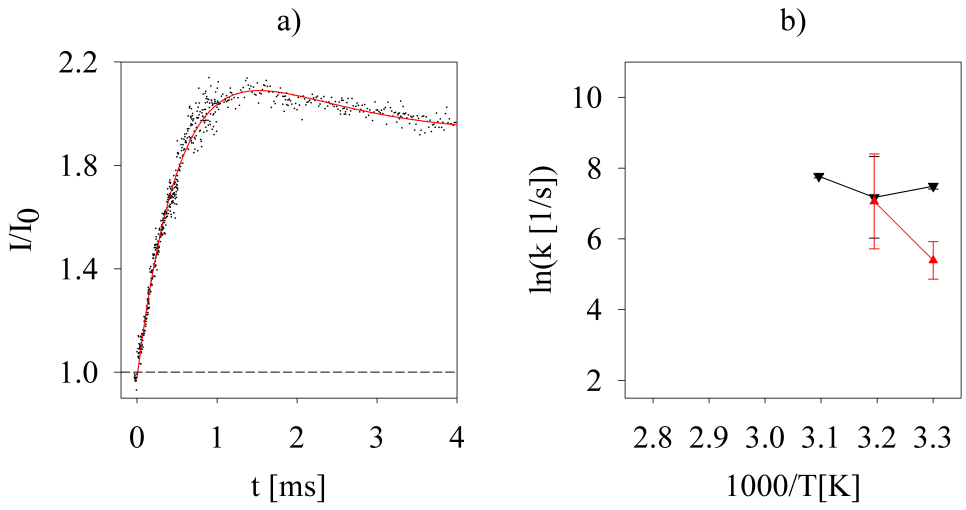

Figure 4.5: a) Intensity curve for VPK-2AP in sodium cacodylate at 40 °C. The plot shows the ratio of our folding and control measurements (without counterions). The fit (red line) is a double exponential fit. The fit looks similar to figure 4.4a. b) Arrhenius plot for VPK-2AP in NaC. The fast rate doesn't show a dependency on temperature, whereas the slower decay rate is decreasing for higher temperatures. For 50 °C almost no decline in intensity can be seen after the initial rise. Therefore this data point was taken out of the Arrhenius plot.

While we could only resolve the slower decay for F-VPK in NaC, the intensity curves for VPK-2AP under the same conditions show a slightly longer formation process and a decay afterwards, as can be seen in figure 4.5a. Measurements were done at 30, 40 and 50 °C. The decay time increases with temperature. For 50 °C almost no decrease in signal can be seen after the initial rise. The fast formation rate is almost constant. The rates and Arrhenius plot are shown in table 4.3 and 4.5b, respectively.

Table 4.3: Folding rates and times for VPK-2AP in NaC based on a double exponential fit to the data. All points after 10 μs were included for the fit.

	T in °C	k in 1/s	Δk in 1/s	τ_f in s	$\Delta\tau$ in s
fast rate	30	1800	100	5.6E-04	5.E-05
	40	1000	2000	8.E-04	9.E-04
	50	2400	100	4.2E-04	2.E-05
slow rate	30	220	100	5.E-03	2.E-03
	40	1200	2000	1.E-03	1.E-03
	50	30	500	3.E-02	4.E-01

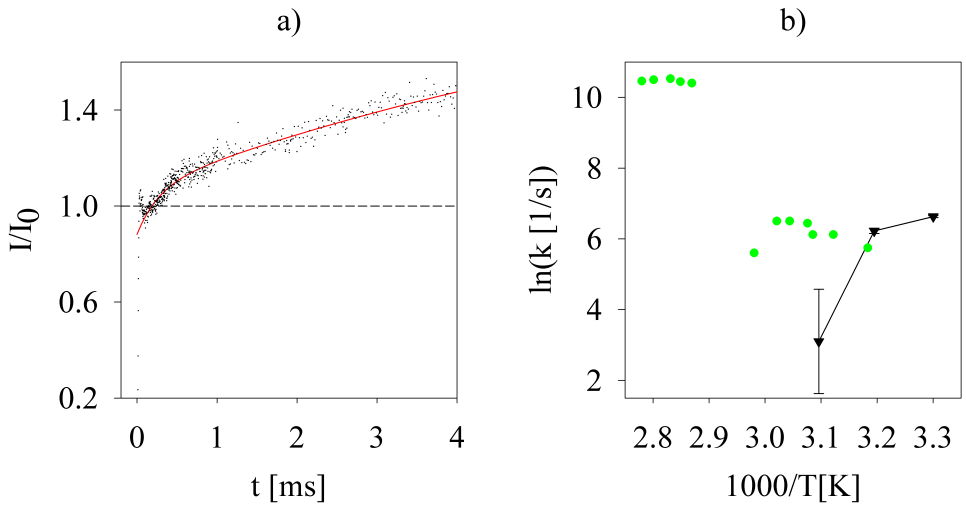

Figure 4.6: a) Intensity curve for VPK-2AP in MOPS at 40 °C. The plot shows the ratio of our folding and control measurements (without counterions). The fit is a single exponential formation process. There might be an early folding process within mixing time. b) Arrhenius plot for VPK-2AP in MOPS. The formation for 50 °C is very slow and we cannot determine its rate precisely. The green circles are data points taken by Velmurugu et al. [46].

Finally, for VPK-2AP in MOPS the data shows only a rise in intensity. The intensity plot for 40 °C is shown in figure 4.6a. Again, data was taken at 30, 40 and 50 °C. The Arrhenius plot can be seen in figure 4.6b. The folding times are exposed in table 4.4, showing an increase with temperature. The data for the 50 °C measurement indicates a very slow rate which we cannot resolve accurately resulting in a high uncertainty of the fit.

Table 4.4: Folding rates and times for VPK-2AP in MOPS based on a single exponential fit to the data. All points after 10 μs were included for the fit.

T in °C	k in 1/s	Δk in 1/s	τ_f in s	$\Delta\tau$ in s
30	750	20	1.32E-03	4.E-05
40	500	40	2.0E-03	1.E-04
50	20	30	5.E-02	7.E-02

4.3 Discussion

The folding kinetics of RNA pseudoknot VPK have been investigated recently by two other groups. Cho et al. simulated the folding process of VPK in a coarse grained molecular dynamics simulation [45]. In their simulation they generated an ensemble of unfolded conformations at a temperature above the highest melting temperature. Folding is triggered by suddenly reducing the temperature in the simulation to a level below the lowest melting temperature. They reported a hierarchical mechanism with parallel folding pathways. The formation of one loop initiates the folding process. VPK has two stems with distinct stabilities. In terms of free energy stem 1 (cf. figure 4.1) is about 3.8 kcal/mol more stable than stem 2, resulting in a dominating pathway where stem 1 forms before stem 2 with a probability of 77 %. Corresponding to these different stabilities Cho et al. determined the folding time for stem 1 and stem 2 to be about 0.4 ms and 4.3 ms, respectively [45].

Recently Narayanan et al. confirmed these theoretical predictions in a T-jump experiment [7]. They measured folding times of about 0.95 ms and 4.3 ms. This is in very good agreement with the simulation data. As discussed in chapter 3.5, theoretically slightly shorter folding times for ion-jump experiments compared to T-jump are predicted; experimentally, however, the opposite was shown.

Our folding conditions were chosen so as to be able to compare our results with the aforementioned studies. However, a direct comparison between the experiments in 10 mM MOPS with 50 mM KCl and 10 mM NaC with 1 M NaCl might not be possible. Vieregg et al. measured a slight difference in RNA hairpin stability and folding rate depending on whether potassium or sodium cations were present [47].

While for all of our experiments, except for VPK-2AP in MOPS, we could see at least two kinetic phases, we were not able to resolve all of them properly. This was partly because the corresponding folding event started already within the dead time of our mixer, partly due to our limit to follow the folding process only until 4 ms after mixing due to the length of the exit channel.

The Arrhenius-plots of our folding rates shown in the previous section do not have the chevron-shape shown in figure 2.3. This is in agreement with measurements on VPK-2AP in MOPS by Narayani (cf. figure 4.4b). The absence of a chevron-look is probably due to a very small difference in free energy for the different temperatures.

Melting profiles showing equilibrium intensity measurements for VPK-2AP and F-VPK at different temperatures were taken by Velmurugu et al. [46]. Figure 4.7 shows the melting profile for VPK-2AP in 1 M NaCl. The transitions at 51 and 77 °C are attributed to the melting of the pseudoknot stems. In our experiments we observe the folding process from extended to native conformation. Therefore we should read the melting plots from right to left and stop at the temperature at which the experiment was conducted.

Read in such a way, for 30 °C the intensity should go up significantly and decrease slightly at the end. For 40 and 50 °C the final decrease should be smaller and almost disappear. This is exactly what our intensity data for VPK-2AP in NaC (with 1 M NaCl) looks like (figure 4.8). We identify the fast increase in intensity as the formation of stem 2 of pseudoknot VPK upon an already formed stem 1, while the slower decay is due to the alternative folding pathway in which stem 1 forms after stem 2. In agreement with the equilibrium data, the alternative folding pathway vanishes for higher temperatures, since stem 2 melts at around 50 °C. A schematic drawing of the two pathways can be seen in figure 5.1.

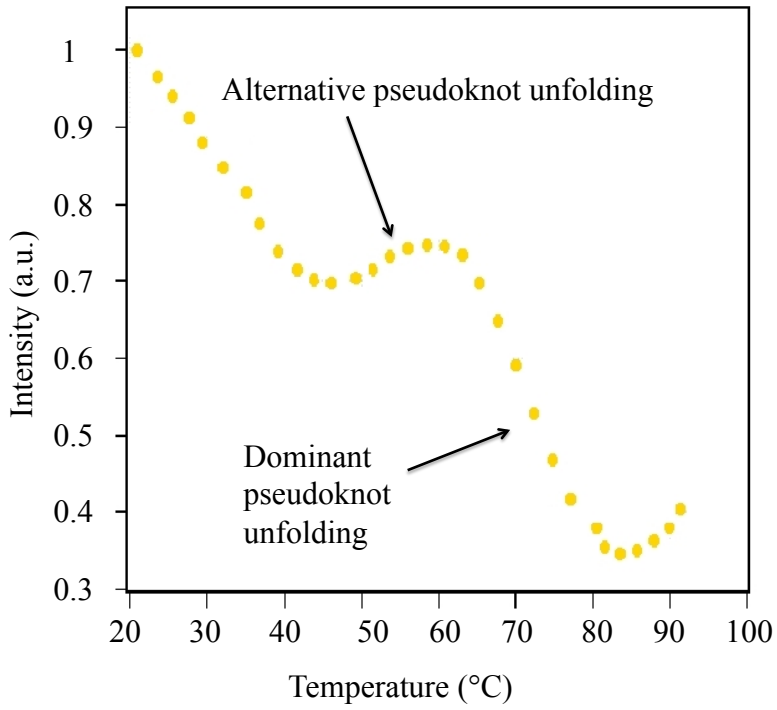

Figure 4.7: Fluorescence melting profile for VPK-2AP in 1 M NaCl.

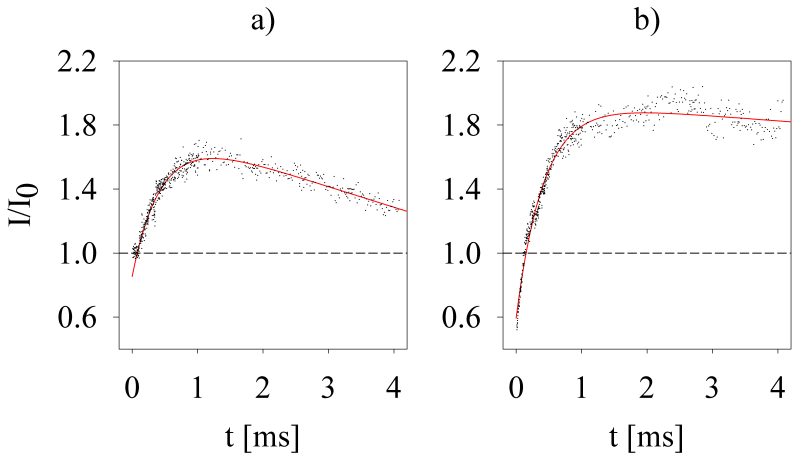

Figure 4.8: Intensity traces for VPK-2AP in NaC for 30 (a) and 50°C (b).

Comparing the melting profile for VPK-2AP in 50 mM KCl, shown in figure 4.9, with our intensity measurements in MOPS (figure 4.10) gives a good match as well. Coming from the unfolded state, the intensity increases steadily for the melting profile as well as our intensity measurements at 30, 40 and 50 °C. The latter shows less final intensity for higher temperatures just as the melting profile suggests. Our 40 °C measurement even indicates a hint of an initial decrease, possibly attributable to folding of the residual hairpins. Our interpretation is that within dead time of the mixer stem 1 forms and fluorescence is reduced because 2AP is in a stacked conformation. The subsequent relaxation shows an increase in fluorescence due to the forming of stem 2.

For F-VPK in 50 mM KCl the melting profile is shown in figure 4.11. Again there is a qualitative agreement between melting profile and intensity curves (figure 4.12). Only the rate for the decay in the signal after the initial rise is very slow, so that we can not resolve the final pseudoknot folding step very well. If we were able to investigate for a longer time after mixing, we might be able to see the decrease in intensity more clearly. Comparing our 30 and 50 °C measurements with the melting profile a similarity between melting profile and our data is apparent.

Unfortunately we do not have a melting profile for F-VPK in 1 M NaCl. The good agreement of the conditions discussed above, however, provides good evidence for the match between the equilibrium melting profiles reported by Velmurugu et al. and our intensity measurements during the folding process [46].

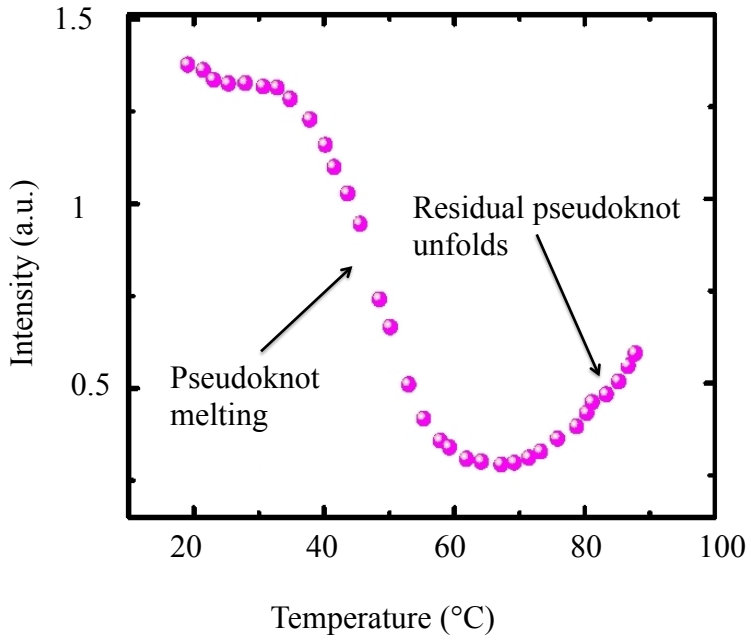

Figure 4.9: Fluorescence melting profile for VPK-2AP in 50 mM KCl.

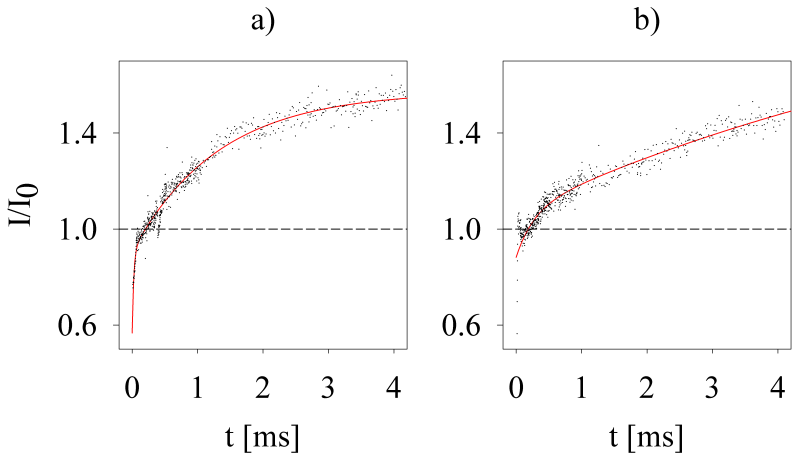

Figure 4.10: Intensity traces for VPK-2AP in MOPS for 30 (a) and 40°C (b).

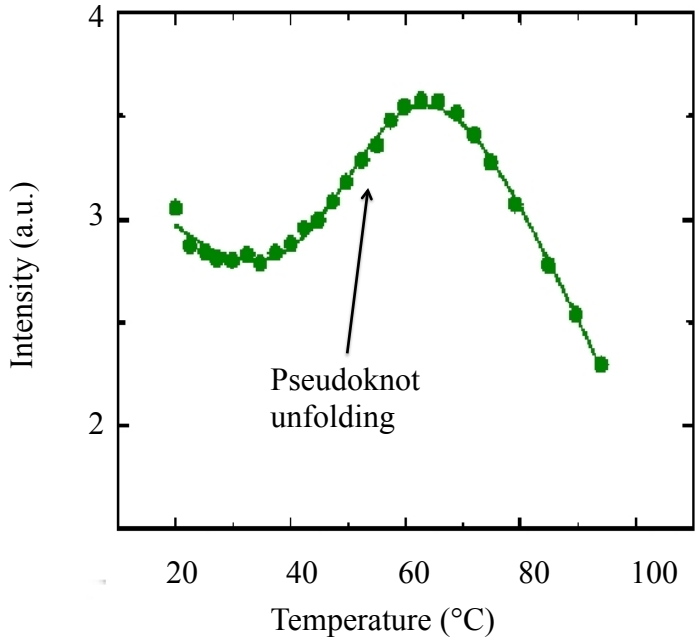

Figure 4.11: Fluorescence melting profile for F-VPK in 50 mM KCl.

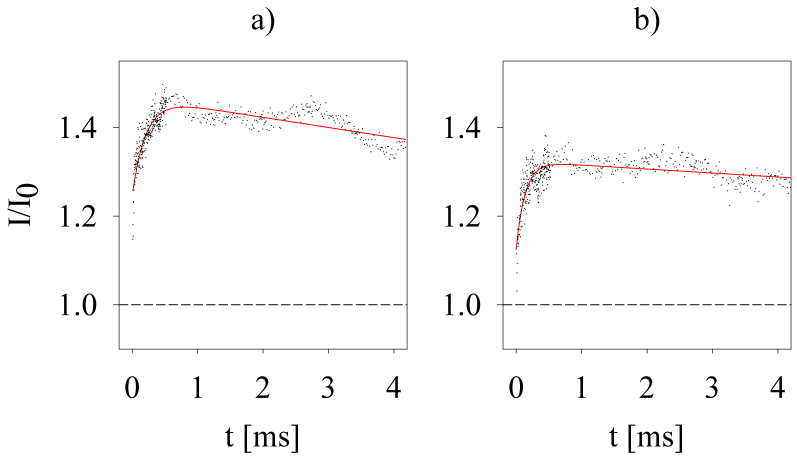

Figure 4.12: Intensity traces for F-VPK in MOPS for 30 (a) and 50°C (b).

As described in the previous section, we fitted single or double exponential functions to our data and thus extracted folding rates. After showing that our data shows behavior similar to the equilibrium data, an interesting question is: How do our folding times compare with T-jump experiments and simulations?

Narayanan et al. published folding rates for F-VPK in 50 mM KCl at 37 °C of 1 - 6 ms [7], while the simulation of Cho et al. predicts folding times of 0.4 and 4.3 ms belonging to the two folding pathways mentioned above. Velmurugu et al. report two folding times for unlabeled VPK in 1 M NaCl, obtained by absorbance measurement after T-jump perturbations, to be around 0.2 - 0.4 ms and $\approx$ 2 ms.

Our data for F-VPK in 10 mM MOPS and 50 mM KCl, summarized in table 4.2, shows two characteristic times, too, having a quick rise followed by a slow decay. The fast folding time doesn't seem to be changing significantly with temperature. Averaging its value from the different measurements the first phase of folding happens after 0.4 ms. The folding times for the slow decay are all within a few milliseconds. For 35 °C it is about 6 ms, for 40 °C it is 1 ms. Both values are close to the previously reported value of 4 ms.

Closest to unlabeled VPK in 1 M NaCl is our VPK-2AP measurement in NaC. A fast folding event happens after around 0.5 ms, followed by a second transition at roughly 4 - 8 ms. The latter folding time is not well resolved and should be treated with caution, though. VPK-2AP in MOPS shows only one transition happening after 1 - 2 ms.

Earlier, Theimer and Giedroc reported two different pairs of melting temperatures for pseudoknot VPK for two monovalent salt conditions, 50 mM KCl and 1 M NaCl [48]. They attributed the higher melting temperature to unfolding of the less stable stem 2, the lower to the more stable stem 1. For 50 mM KCl the two transitions were at 48 and 80 °C,

while for 1 M NaCl these temperatures were shifted to higher temperatures, 70 and 95 °C. Monovalent salt in the environment therefore stabilizes the pseudoknot structure. This conclusion was confirmed by Holmstrom et al. [49]. Investigating the relationship between formation of tertiary structure (a tetraloop-receptor) and Na^+ concentration, they found a clear relationship between salt concentration and the folding and unfolding rate: the higher the concentration the larger (smaller) the folding (unfolding) rate.

Although the size of the counterions seems to have a slight effect on the folding rates, a comparison of our results for the two folding conditions agrees with the general finding that the higher the monovalent salt concentration is, the shorter are the folding times. Having a look at VPK-2AP in NaC and MOPS, respectively, the early folding process for the higher concentration occurs after around 0.6 ms, while for the lower one it starts only after 1 - 2 ms. Similarly for F-VPK at high salt concentration we cannot resolve the early folding process, but we can deduce that it is completed within the first 200 μs. For the lower concentration the folding time is roughly 0.4 ms.

Chapter 5

Summary and outlook

Our folding experiments of RNA pseudoknot VPK exhibit different behaviors for different solvent and labels. Overall, equilibrium melting plots and our folding traces match quite well. This seems surprising, since we did not expect to see this adiabatic behavior in our fast-folding experiment. For VPK-2AP in high salt concentration (1 M NaCl) we interpret our data as showing two different folding pathways (see figure 5.1), while in low salt concentration we can see only one transition. There could be two explanations for the "missing" transition: either one of the stems forms within dead time of our instrument, or it forms on a longer timescale than we can observe. We think the former is more likely, since according to the equilibrium melting profile, the formation of the first hairpin loop occurs at high temperature with a decay in fluorescence signal. Suppose that this formation happens within mixing time, then indeed we wouldn't see a drop in intensity, if drop and subsequent recovery both take place very fast. The characteristic folding times are approximately 1 - 2 ms for the low and 0.5 ms and 4 - 8 ms for the high salt concentration, respectively.

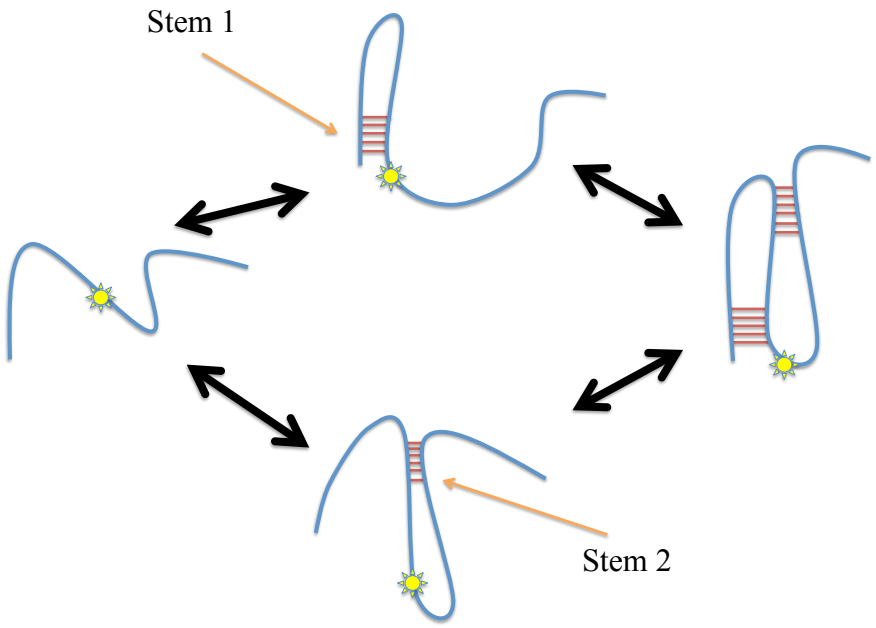

Figure 5.1: Schematics of the folding pathway for VPK-2AP in sodium cacodylate with 1 M NaCl. The position of the intrinsic fluorescence label 2-AP is indicated by the small sun. The base pairing regions of stems 1 and 2 are drawn in red. The upper pathway represents the dominant folding pathway, where stem 1 forms first followed by stem 2.

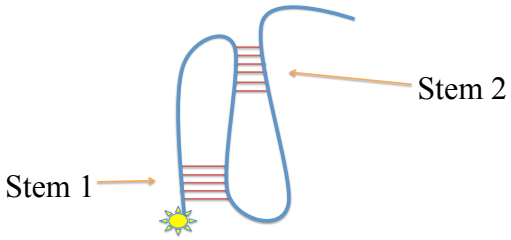

Figure 5.2: Schematics of VPK-F. The fluorescein label is at the 5'-end of the RNA, close to stem 1 of the pseudoknot. It seems unclear, why the forming of stem 2 should have an effect on the fluorescence signal.

For the fluorescein-labeled F-VPK in high salt concentration we observed an initial strong increase in fluorescence within dead time of our mixer, followed by a steep decline on a time scale of around 0.6 ms. The decline could possibly consist of two processes, but we cannot tell for sure. For the lower salt concentration we detected two folding phases. This is in agreement with the equilibrium melting profiles for F-VPK. However, Velmurugu et al. interpreted the decrease in fluorescence for higher temperatures as a temperature dependent response of the fluorescein label [46]. Our kinetic data seems to provide evidence for another transition in the RNA. At this time, we are not sure of the nature of this transition. It might be due to a parallel folding pathway just the same as for VPK-2AP. But we cannot tell yet, why the forming of stem 2 should affect the fluorescence signal of the fluorescein label attached at the far other end of the RNA strand (see figure 5.2).

2-AP is very sensitive for different environments and shows different fluorescence properties even for nearest neighbours [50]. Including 2-AP labels at different positions could be a way to rule out different folding pathways. Additionally, in order to rule out a change in

signal due to the mixing of 2-AP in the folding buffer, measurements of 2-AP alone should be done.

Vieregg et al. showed that the size of the counterions matters in terms folding rate [47]. It could prove insightful to conduct measurements at different concentrations of the same salt. This would make direct comparisons of different salt conditions possible. Also, a more detailed investigation of the influence the size of counterions has on the RNA folding process could reveal interesting findings and be helpful for the analysis of further experiments in the future.

BIBLIOGRAPHY

BIBLIOGRAPHY

[1] I. Tinoco Jr. and C. Bustamante, J. Mol. Biol. **293**, 271 (1999).

[2] P. G. Higgs, Q. Rev. Biophys. **33**, 199 (2000).

[3] W. Gilbert, Nature **319**, 618 (1986).

[4] J. Carter and V. Saunders, *Virology: Principles and Applications*; Wiley: Chichester, 2007; page 32.

[5] H. Yang, M. Yang, Y. Ding, Y. Liu, Z. Lou, Z. Zhou, L. Sun, L. Mo, S.Ye, H. Pang, G. F. Gao, K. Anand, M. Bartlam, R. Hilgenfeld, and Z. Rao, PNAS **100**, 1390 (2003).

[6] G. Neumann, T. Noda, and Y. Kawaoka, Nature **459**, 931 (2009).

[7] R. Narayanan, Y. Velmurugu, S. G. Kuznetsov, and A. Ansari, J. Am. Chem. Soc. **133**, 18767 (2011).

[8] C. Branden and J. Tooze, *Introduction to Protein Structure*; Garland Publishing, Inc.: New York, 1999; Chapter 2 and 6.

[9] M. Sela, F. H. White, and C. B. Anfinsen, Science **125**, 691 (1957).

[10] S. B. Prusiner, Science **278**, 5336 (1997).

[11] L. M. Luheshi, D. C. Crowther, and C. M. Dobson, Curr. Opin. Chem. Biol. **12**, 25 (2008).

[12] D. E. Draper, Biophys. J. **95**, 5489 (2008).

[13] J. R. Wyatt, J. D. Puglisi, and I. Tinoco Jr., BioEssays **11**, 100 (1989).

[14] R. Zwanzig, PNAS **94**, 148 (2005).

[15] A. D. Robertson and K. D. Murphy, Chem. Rev. **97**, 1251 (1997).

[16] Martin Karplus, Nat. Chem. Biol. **7**, 401 (2011).

[17] A. Szilagyi, J. Kardos, S. Osvath, L. Barna, and P. Zavodszky, Protein Folding. In *Handbook of Neurochemistry and Molecular Neurobiology*, A. Lajtha and N. Banik, Eds.; Springer: New York, 2007; Vol. 7, Chapter 10, pp. 303-344.

[18] J. N. Onuchic, Z. Luthey-Schulten, and P. G. Wolynes, Annu. Rev. Phys. Chem. **48**, 545 (1997).

[19] K. A. Beauchamp, R. McGibbon, Y. Lin, and V. S. Pande, PNAS 10.1073/pnas.1201810109 (published ahead of print July 9, 2012).

[20] A. B. Fulton and W. B. Isaacs, BioEssays **13**, 157 (1991).

[21] C. Levinthal, How to fold Graciously. In *Mossbauer Spectroscopy in Biological Systems: Proceedings of a meeting held at Allerton House, Monticello, Illinois*, J. T. P. DeBrunner and E. Munck, Eds., University of Illinois Press: Champaign, 1969; pp. 22-24.

[22] V. Pande and Stanford University (2012), *The Science behind Folding@home*. Retrieved from http://folding.stanford.edu/English/Science.

[23] K. Lindorff-Larsen, S. Piana, R. O. Dror, and D. E. Shaw, Science **334**, 517 (2011).

[24] D. E. Shaw, M. D. Deneroff, R. O. Dror, J. S. Kuskin, R. H. Larson, J. K. Salmon, C. Young, B. Batson, K. J. Bowers, J. C. Chao, M. P. Eastwood, J. Gagliardo, J. P. Grossman, C. R. Ho, D. J. Ierardi, I. Kolossvry, J. L. Klepeis, T. Layman, C. McLeavey, M. A. Moraes, R. Mueller, E. C. Priest, Y. Shan, J. Spengler, M. Theobald, B. Towles, and S. C. Wang, Comm. of the ACM **51**, 91 (2008).

[25] V. Pande and Stanford University (2012), *Folding@home*. Retrieved from http://folding.stanford.edu/English/HomePage.

[26] H. A. Scheraga, M. Khalili, and A. Liwo, Annu. Rev. Phys. Chem. **58**, 57 (2007).

[27] J. Kubelka, J. Hofrichter, and W. A. Eaton, Curr. Opin. Struct. Biol. **14**, 76 (2004).

[28] T. R. Sosnick, Protein Sci. **17**, 1308 (2008).

[29] W. A. Eaton, V. Munoz, S. J. Hagen, G. S. Jas, L. J. Lapidus, E. R. Henry, and J. Hofrichter, Annu. Rev. Biophys. Biomol. Struct. **29**, 327 (2000).

[30] R. H. Webb, Rep. Prog. Phys. **59**, 427 (1996).

[31] M. W. Davidson (2012), *Basic Concepts and Formulas in Microscopy.* Retrieved from http://www.microscopyu.com/articles/formulas/formulasresolution.html.

[32] K. R. Spring, T. J. Fellers, and M. W. Davidson (2009), *Resolution and Contrast in Confocal Microscopy.* Retrieved from http://www.olympusconfocal.com/theory/resolutionintro.html.

[33] J. B. Knight, A. Vishwanath, J. P. Brody, and R. H. Austin, Phys. Rev. Lett. **80**, 3863 (1998).

[34] L. Capretto, W. Cheng, M. Hill, and X. Zhang, Top. Curr. Chem. **304**, 27 (2011).

[35] N.-T. Nguyen and S. T. Wereley, *Fundamentals and Application of Microfluidics*; Artech House, Inc.: Norwood, 2002, p. 39.

[36] L. J. Lapidus, S. Yao, K. S. McGarrity, D. E. Hertzog, and E. Tubman, Biophys. J. **93**, 218 (2007).

[37] D. E. Hertzog, X. Michalet, M. Jäger, X. Kong, J. G. Santiago, S. Weiss, and O. Bakajin, Anal. Chem. **76**, 7169 (2004).

[38] J. Kubelka, Photochem. Photobiol. Sci. **8**, 499 (2009).

[39] S. Biyun, S. S. Cho, and D. Thirumalai, J. Am. Chem. Soc. **133**, 20634 (2011).

[40] R. Narayanan, L. Zhu, Y. Velmurugu, S. V. Kuznetsov, L. Lapidus, and A. Ansari (2012) *Exploring the energy landscape of nucleic acid hairpins using laser temperature-jump and microfluidic mixing.* Manuscript submitted for publication.

[41] L. X. Shen and I. Tinoco, Jr, J. Mol. Biol. **247**, 963 (1995).

[42] I. Brierley, S. Pennell, and R. G. C. Gilbert, Nat. Rev. Microbiol. **5**, 598 (2007).

[43] J. M. Jean and K. B. Hall, PNAS **98**, 37 (2000).

[44] U. D. Priyakumar, C. Hyeon, D. Thirumalai, and A. D. MacKerell, Jr, J. Am. Chem. Soc. **131**, 17559 (2009).

[45] S. S. Cho, D. L. Pincus, and D. Thirumalai, PNAS **106**, 17349 (2009).

[46] Y. Velmurugu, R. Narayanan, J. Roca, J. Liu, S. V. Kuznetsov, and A. Ansari, *Laser T-jump studies of RNA pseudoknots reveal parallel folding/unfolding pathways*. Poster session presented at: Gordon Research Conferences 2012. Biopolymers - In Vitro, In Silico, and in the Cell. June 3-8, 2012. Newport, RI.

[47] J. Viergg, W. Cheng, C. Bustamante, I. Tinoco, Jr., J. Am. Chem. Soc. **48**, 14966 (2007).

[48] C. A. Theimer and D. P. Giedroc, RNA **6**, 409 (2000).

[49] E. D. Holmstrom, J. L. Fiore, and D. J. Nesbitt, Biochem. **51**, 3732 (2012).

[50] K. B. Hall and F. J. Williams, RNA **10**, 34 (2000).